Overturned internal capillary-gravity waves

Benjamin F. Akers David M. Ambrose Kevin Pond J. Douglas Wright

June 30, 2015

Abstract

A vortex sheet formulation of irrotational, incompressible Euler flow is used to compute periodic traveling waves at the interface between two constant-density, two-dimensional fluids, including waves with overturned crests. Branches of traveling waves are computed via numerical continuation, which are jointly continuous in the physical parameters: Bond number, Atwood number and mean shear. Global branches are computed, for various choices of parameters, illustrating the termination criteria of the global bifurcation theorem of [1]. Small amplitude asymptotics of traveling waves are calculated. The role of the wave's second harmonic in determining crest/trough shape is discussed. Waves of extremal displacement and those approaching self-intersection are computed. Surfaces in parameter space indicating where traveling waves exist are computed; these surfaces themselves have both overturned and self-intersecting boundaries.

1 Introduction

We study the irrotational, incompressible Euler equations at the interface between two constant-density fluids; these are an upper fluid and a lower fluid. The fluid regions are infinitely deep in the vertical direction and periodic in the horizontal direction. We seek traveling wave solutions, or solutions for which the free surface is of permanent form and steadily translating. Waves are computed on this interface numerically, including the effects of the physical parameters of surface tension, gravity, mean shear, and density ratio. We compute large amplitude solutions, including those with overturned crests or troughs, up to the limit of self-intersection.

Since the fluids are irrotational in the bulk, the vorticity is equal to zero inside either fluid region. The velocity may jump at the interface (specifically, the tangential component of the velocity may jump, while the normal component must be continuous) [2], thus, the vorticity is not identically zero but is instead measure-valued and supported only on the interface. The interface is thus referred to as a vortex sheet.

We denote the densities of the fluids as ρ_1 and ρ_2, which can each be any non-negative, constant value (not both zero). A useful non-dimensional quantity, then, is the Atwood number, $\mathrm{At} = (\rho_1 - \rho_2)/(\rho_1 + \rho_2)$. The surface tension parameter is τ, which is taken to be a positive constant, and the constant acceleration due to gravity is g, which may be any real value.

The present work extends prior work by three of the authors. In [3], a novel formulation for the interfacial traveling wave problem was introduced, and was used for both analysis and computing. In particular, in the case in which the two fluids have equal density (i.e., $\mathrm{At} = 0$), a local bifurcation theorem was applied to show the existence of small-amplitude traveling waves, for any value of the mean shear, for fixed, nonzero surface tension. Numerical solutions were computed using a quasi-Newton method in Fourier space, similar to [4]. Subsequently, the same authors followed up in [5], in which water waves were studied. The water wave is the special case of the vortex sheet in which the upper fluid is taken to have density equal to zero (i.e., $\mathrm{At} = 1$); the gravity parameter was able to be taken to be positive, negative, or zero. The analysis of this work used the implicit function theorem to demonstrate that Crapper waves [6], which are a family of exact, pure capillary traveling water waves, can be perturbed through the inclusion of gravity; see also [7], [8] for further developments in this area. The computational portion of [5] again used a quasi-Newton method in Fourier space to compute these gravity-perturbed Crapper waves; a new wave of maximum amplitude was found when the gravity parameter takes a specific small, negative value.

Further analysis has since been carried out by two of the authors and Strauss [1]. In this work, a global bifurcation theorem was proved, allowing arbitrary densities. In the case that the two fluids have different densities, the main theorem of [1] specializes to the following:

Theorem 1 *For all choices of the surface tension parameter $\tau > 0$, the spatial periodicity parameter $M > 0$, the mean shear parameter $\gamma_0 \in \mathbb{R}$, the densities of the fluids $\rho_1, \rho_2 \geq 0$ (with $\rho_1 \neq \rho_2$) and the gravity parameter $g \in \mathbb{R}$, there exists a countable number of connected sets of smooth non-trivial symmetric periodic traveling wave solutions (bifurcating from a quiescent equilibrium) for the two-dimensional gravity-capillary vortex sheet problem. Each of these connected sets has at least one of the following properties:*

(a) it contains waves whose interfaces have lengths which are arbitrarily long;

(b) it contains waves whose interfaces have curvature which is arbitrarily large;

(c) it contains waves where the jump in the tangential component of the fluid velocity across the interface or its derivative is arbitrarily large;

(d) its closure contains a wave whose interface contains a point of self intersection;

(e) it contains a sequence of waves whose interfaces converge to a flat configuration but whose speeds contain at least two convergent subsequences whose limits differ.

One might say that a shortcoming of the theory of global bifurcations is that, while a variety of possible behaviors along bifurcation curves can be identified, the theory does not generally identify which of these behaviors in fact occur. We thus address this question via simulation. We have been able to find all of the behaviors, (a) through (e), computationally, for some choices of parameter values. For example, cases (a), (b), and (c) all occur in the density matched cases, and are reported in [3]. Case (d) occurs at the generic choice of parameter values in this work, and is well known to occur for the Crapper family of waves ($\mathrm{At} = 1$, $g = 0$) [6]. The most controversial is case (e), since in analytical work in the absence of surface tension, this phenomenon can typically be ruled out by a maximum principle argument; one example of such an argument is in [9]. In the presence of surface tension, the maximum principle argument is not available because of the larger number of derivatives. We find that outcome (e) can occur for certain negative values of the gravity parameter; this is illustrated in Figure 1.

There are numerous studies of the similar problem without surface tension. For example, the case of $\tau = 0$ with At varying has been numerically studied by Vanden-Broeck and Turner [10, 11]. They observe that the maximal waves are near turning points in the speed-amplitude plane (i.e.,

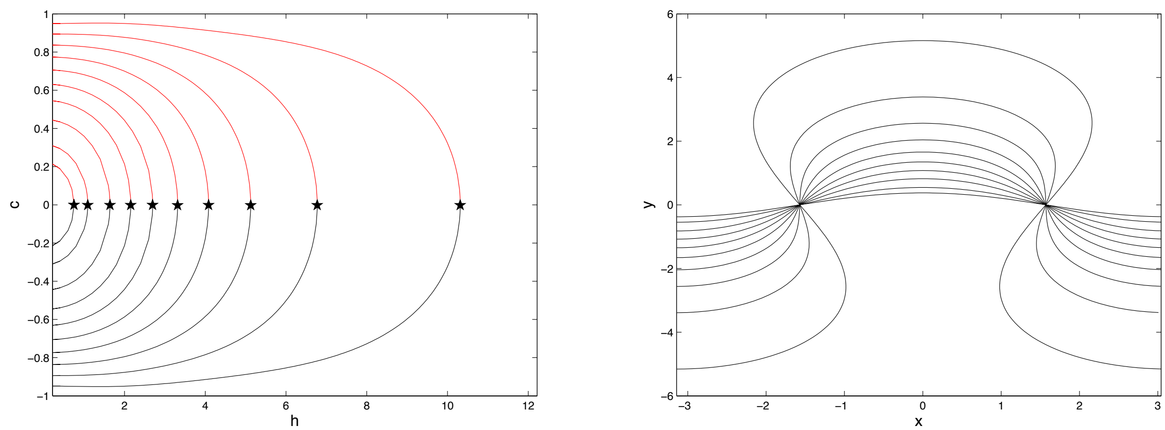

Figure 1: Examples of branches of waves in case (e) of the global bifurcation theorem, where the flat state at one speed is connected to the flat state at another speed. The numerically computed branches, curves relating speed c and displacement, $h = \max(y) - \min(y)$, are on the left. The largest amplitude profiles are standing waves ($c = 0$). These standing waves are marked by stars in the left panel, and have profiles depicted in the right panel. All branches are computed with $\tau = 2, \mathrm{At} = 0.5$, and the Bond number varies between branches: $\sigma \in [-1.8, -0.09]$. (The Bond number is defined in Section 2.)

the bifurcation curves spiral in). Another early study is by Meiron and Saffman with $\tau = 0$ and different values of At.

With surface tension, the special cases $\mathrm{At} \in \{0, 1\}$ have been studied several times, including, as we have mentioned, by some of the authors in [3, 5, 1]. Modern studies of the case $\mathrm{At} = 1$, with small surface tension $\tau \approx 0$, include both the infinite [12] and finite depth cases [13]. A host of classical and overturned traveling water waves ($\mathrm{At} = 1$) have been computed by Okamoto and colleagues, many of which are presented in the manuscript [14]. Our numerical work differs in flavor from much of that in the literature in our focus on the global bifurcation picture, computing the location in parameter space of waves of extremal displacement and self intersection. The numerical methods described herein require that the vortex sheet does not self intersect; traveling waves can be computed with self intersections (or bubbles) via other methods, see [15].

Other works have considered the case of two fluids, an upper layer of finite depth and a vacuum above; in this setting, there is an interface between the two fluids, and an upper free surface [16, 17]. Finally, we mention that there are also experimental works on this subject, such as [18, 19, 20, 21]. Of course, in addition to periodic traveling waves, solitary waves are also considered, for example in the numerical work [22].

The works just described all considered the Euler equations. Of course, in interfacial fluid dynamics, there are also many approximate models which have been developed, such as the Korteweg-de Vries equation and the Benjamin-Ono equation, among others. Some relevant papers using model equations are [23, 24, 25, 26]. Another kind of approximation technique is amplitude expansion methods; the papers [27, 28, 29, 30] make such expansions in the manner of Stokes. The beginnings of an amplitude expansion for internal waves on the vortex sheet are derived herein.

The remainder of the paper is organized as follows. In Section 2, we will give the equations of motion for our capillary-gravity interfacial fluid problem. This includes giving the traveling wave ansatz, as developed by the authors in [3]. In Section 3, a weakly nonlinear theory is developed, both describing the qualitative nature of small amplitude traveling waves and providing initial guesses for numerical solutions of the full Euler system. In Section 4, our numerical methods are described, including descriptions of two methods for exploring parameter space: one based on adaptive sampling and another which uses continuation to trace the boundaries of where traveling waves exist. Numerical results from these algorithms are given in Section 5. Conclusions and future research areas are presented in Section 6.

2 Formulation

We start from the formulation developed by the same authors in [3, 5], which we now describe. The traveling wave equations are derived from the evolution equations for a vortex sheet at the interface of two incompressible irrotational fluids. As with any free boundary problem, both the interface and its evolution must be described. We write the free surface as $(x(\alpha,t), y(\alpha,t))$, define its normal velocity to be U, and its tangential velocity to be V. The normal velocity of the fluid on the interface is $W\cdot\hat{n}$, which must match the interface normal U for continuity. The tangential velocity of the fluid on the interface is $W\cdot\hat{t}$, which appears in the evolution equation for the vortex sheet strength (1), but need not match V. We choose to describe the interface motion in terms of its vortex sheet strength $\gamma(\alpha,t)$ and tangent angle $\theta = \arctan(y_\alpha/x_\alpha)$. In terms of these variables, the change in vortex sheet strength is

$$\gamma_t = \frac{2\pi}{L}\theta_{\alpha\alpha} + \frac{2\pi}{L}((V-W\cdot\hat{t})\gamma)_\alpha - 2\mathrm{At}\left(\frac{2\pi}{L}W_t\cdot\hat{t} + \frac{\sigma L}{2\pi}\sin(\theta) + \frac{\pi^2}{L^2}\gamma\gamma_\alpha - (V-W\cdot\hat{t})(W_\alpha\cdot\hat{t})\right). \quad (1)$$

The parameter $\sigma = \frac{g}{k^2\tau}$ is the Bond number, measuring the relative importance of gravity to surface tension (in which k is the typical wavenumber); the number $\mathrm{At} = \frac{\rho_1-\rho_2}{\rho_1+\rho_2}$ is again the Atwood ratio comparing the densities of the upper and lower fluids. The length of the interface over one period is L, in a dimensionless coordinate system where the horizontal period of the wave is 2π. The water wave problem can be studied by setting $\mathrm{At}\approx 1$, whereas internal oceanic waves and atmospheric vortex sheets have $\mathrm{At}\approx 0$. Equation (1) states that changes in vortex sheet strength occur due to curvature of the surface, advection of the vortex sheet strength, inertia, and gravitational forces. A full derivation of equation (1) from the potential flow equations can be found in [2].

The function W is complexification of the fluid velocity at the free surface, defined by the closure

$$\overline{W} = \frac{1}{4i\pi}\mathrm{PV}\int_0^{2\pi}\gamma(\alpha',t)\cot\left(\frac{1}{2}(z(\alpha)-z(\alpha'))\right)\,d\alpha', \quad (2)$$

with $z(\alpha) = x(\alpha)+iy(\alpha)$ being the complexified location of the free surface. As noted in [31], the tangential velocity of the interface is not a physical quantity, and need not match the tangential velocity of the fluid particles one the interface. Thus we are free to adjust the tangential velocity of the surface, for example to preserve an arclength based parameterization, as we do here via

$$V_\alpha = U\theta_\alpha. \quad (3)$$

Paired with equation (1) is the kinematic equation,

$$\theta_t = U_\alpha + V\theta_\alpha. \tag{4}$$

It is the evolution equations (1) and (4), and their closures (2) and (3), that we refer to as the vortex sheet formulation.

We seek traveling waves whose interface has a regular paramterization, but are not necessarily single-valued functions of x. Rather than the traditional traveling wave ansatz, $\theta = f(x - ct)$, we use the method developed in [3, 5] (see also [1]), which instead imposes $x_t = c$, $y_t = 0$. This form of the traveling wave ansatz in turn implies

$$U = -c\sin(\theta), \qquad V = c\cos(\theta), \qquad \text{and} \qquad \gamma_t = 0. \tag{5}$$

With the ansatz (5), traveling waves to the vortex sheet formulation are solutions $(\theta(\alpha), \gamma(\alpha), c)$ of the system

$$\theta_{\alpha\alpha} + ((c\cos(\theta) - W\cdot\hat{t})\gamma)_\alpha - 2\mathrm{At}\left(\frac{\sigma L^2}{4\pi^2}\sin(\theta) + \frac{\pi}{2L}\gamma\gamma_\alpha - \frac{L}{2\pi}(c\cos(\theta) - W\cdot\hat{t})(W_\alpha\cdot\hat{t})\right) = 0, \tag{6a}$$

$$W\cdot\hat{n} + c\sin(\theta) = 0. \tag{6b}$$

(Note that the $W_t = 0$ for traveling waves and thus some terms in (1) disappear.) For the remainder of the paper we discuss solutions of (6), beginning with small amplitude asymptotics, followed by numerical solutions.

3 Weakly Nonlinear Theory

In this section we derive the asymptotics of traveling waves as a series in wave slope, ϵ. The first weakly nonlinear correction to infinitesimal, linear waves is calculated exactly. At this level of approximation, one may predict whether, at small amplitude, the waves have steeper troughs or crests, as noted in [29, 30]. This approximation is used as an initial guess for small amplitude waves in a quasi-Newton numerical solver. In the numerical section that follows, we consider a heuristic based on the small amplitude prediction: Do waves which have steeper crests and flatter troughs at small amplitude have increasingly steep crests as amplitude increases, and are they then limited in amplitude by a wave which entrains a bubble into the *upper* fluid? On the other hand waves with flatter crests and steeper troughs at small amplitude may have increasingly steep troughs as amplitude increases, and could then be limited in amplitude by a wave which entrains a bubble into the *lower* fluid. If this heuristic were valid, then small amplitude asymptotics would predict large amplitude behavior.

To calculate the wave's asymptotics, a Stokes' expansion [32, 33] is directly substituted into (6), assuming

$$\theta = \sum_{n=1}^{\infty}\epsilon^n\theta_n \qquad \gamma = \sum_{n=0}^{\infty}\epsilon^n\gamma_n \qquad c = \sum_{n=0}^{\infty}\epsilon^n c_n.$$

In the non-dimensional form, the linear solutions have wavelength 2π, and non-trivial solutions exist at two phase speeds

$$c_0 = \frac{\mathrm{At}\gamma_0}{2} \pm \sqrt{\frac{1}{2} + \sigma\mathrm{At} - \frac{(1-\mathrm{At}^2)}{4}\gamma_0^2} \tag{7}$$

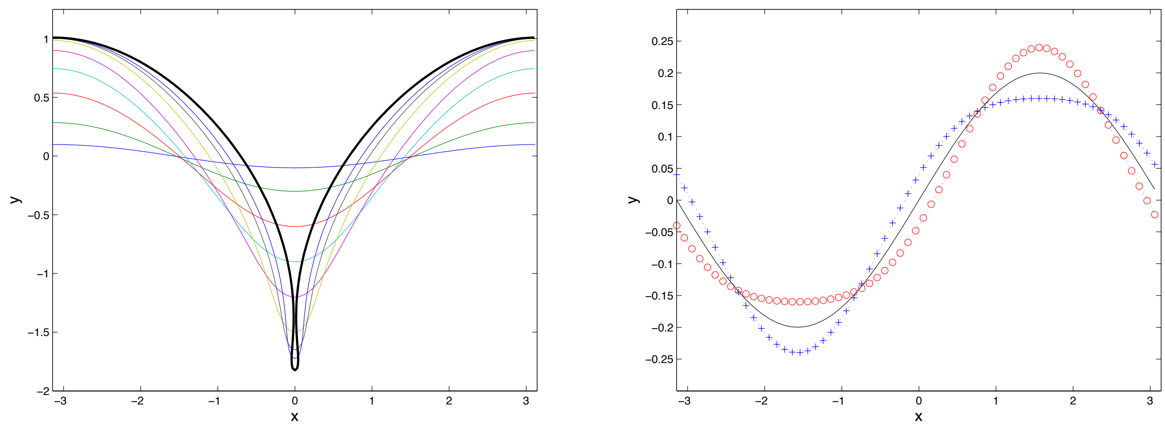

Figure 2: **Left:** Profiles of a typical branch of traveling waves, with $\sigma = \frac{1}{2}, \mathrm{At} = 0.5, \gamma_0 = 0.5$, at a sampling of amplitudes are overlaid. The largest computed profile is marked with the thicker line. **Right:** Wave profiles from equation (10) with $\epsilon = 0.25$ and $d_1 = -1, 0$, and 1, marked with plus signs, a solid line, and circles respectively. When d_1 is positive the profile has steeper troughs and flatter crests; when d_1 is negative the profiles have steeper crests and flatter troughs.

The mean shear, γ_0 cannot be determined from the equations, and should be thought of as a parameter to be specified, like the Bond or Atwood numbers (although not just any value of γ_0 is allowed, as we desire real valued speeds c_0). With phase speed given by (7), the linear solution to (6) can be written as

$$\theta_1 = e^{ix} + * \qquad \text{and} \qquad \gamma_1 = -2ic_0 e^{ix} + *,$$

where the $*$ refers to the complex conjugate of the preceding terms; thus, the solutions are real. Continuing to the next order, for general $\gamma_0, \mathrm{At}, \sigma$, the speed is uncorrected: $c_1 = 0$. We have calculated the corrections to the tangent angle and vortex sheet strength

$$\theta_2 = id_1 e^{2ix} + *, \qquad \text{and} \qquad \gamma_2 = D_1 e^{2ix} + *,$$

with

$$d_1 = \frac{2\gamma_0 c_0 - 2\mathrm{At}c_0^2 - \frac{1}{2}\mathrm{At}\gamma_0^2}{\mathrm{At}\sigma - 1 - \frac{1}{2}\gamma_0^2}, \tag{8a}$$

$$D_1 = \frac{\frac{1}{4}\gamma_0(4\tau + 2\sigma\mathrm{At} - \gamma_0^2) + 3c_0^2\gamma_0 - 4\mathrm{At}c_0^3}{\mathrm{At}\sigma - 1 - \frac{1}{2}\gamma_0^2}. \tag{8b}$$

These corrections are singular, due to a triad resonance, at

$$\gamma_0 = \pm\sqrt{2(\mathrm{At}\sigma - 1)}, \qquad \text{and} \qquad \sigma\mathrm{At} = (1 + \gamma_0^2/2) \tag{9}$$

Notice that neither of these singularities occurs if $\sigma = 0$ (pure capillary waves). The latter singularity is the internal wave analogue of the Wilton ripple [34], due to the interplay of gravity and surface tension, and does not require a mean shear. The former is a shear-based singularity, whose presence suggests the existence of a new type of ripple-like traveling waves. This singularity of the d_1 is not the Kelvin-Helmholtz instability, which happens in this context at wavenumbers satisfying

$$\frac{|k|}{2} + \frac{\sigma \mathrm{At}}{|k|} - \frac{1}{4}(1 - \mathrm{At}^2)\gamma_0^2 < 0$$

The shear-based singularity of d_1 occurs when both $k = 1$ and $k = 2$ are traveling waves based on linear theory *and* neither wavenumber is Kelvin-Helmholtz unstable. In this work we consider parameter values where the denominator is non-singular. The computation of internal wave ripples is planned as an avenue of future study. At the generic, non-resonant, parameter values the interface location is, to $O(\epsilon^2)$,

$$y = 2\epsilon \sin(x) + \epsilon^2 d_1 \cos(2x). \tag{10}$$

In the case of no upper fluid, $\mathrm{At} = 1$, with $\gamma_0 = 0$, the coefficient d_1 reduces to the one reported by Pierson and Fife [35]. The sign of coefficient d_1 determines whether small amplitude solutions have steeper troughs or crests. When this coefficient is negative, waves of increasing amplitude have increasingly steep troughs. When it is positive, waves of increasing amplitude have increasingly steep crests, see Figure 2. Numerically we observe that this behavior continues along a branch of traveling waves, away from $\epsilon = 0$.

In the following sections, we explore the parameter space of traveling waves. We compute global branches and surfaces in parameter space where traveling waves exist. We also test the heuristic that the qualitative nature of self-intersecting wave profiles, whether they include entrained bubbles (into the lower fluid) or drops (into the upper fluid), can be predicted by their small amplitude behavior: whether the small amplitude waves had steeper troughs or crests, respectively, as predicted by the sign of d_1.

4 Numerical Method

The numerical method used to solve system (6) is similar to that of [3, 5]. Fourier-collocation is used to discretize spatial derivatives. We seek symmetric, even profiles in terms of tangent angle θ and vortex sheet strength γ. When the system is discretized with N spatial points, we must then solve for N Fourier modes and the wave speed c. The projection of the partial differential equations into Fourier space gives N equations, to which we append an equation fixing the amplitude to close the system. The resulting nonlinear system of algebraic equations is then solved via a quasi-Newton method, using Broyden's update of the Jacobian [36]. Branches of waves are then computed using continuation in amplitude (or Bond number, Atwood number, or mean shear) similarly to [37, 38].

This method is used to compute traveling waves at various values of displacement $h = \max(y) - \min(y)$, Bond number σ, Atwood number At, and mean shear γ_0. The four-dimensional parameter space (h, σ, At, γ_0) is quite vast. To efficiently explore this space we use two numerical strategies. The first, which assumes continuity of branches of traveling waves only in total displacement, is the adaptive sampling methodology described in the following subsection. In this strategy, the Bond number, Atwood number and mean shear are sampled, and branches of waves are computed in total displacement (depicted by vertical lines in Figure 3). The second method, which we refer to as the boundary continuation method (BCM), uses continuation to trace the boundaries of where traveling waves exist (either the largest wave on a branch or the limit of self intersection). The latter method follows the boundary of where traveling waves exist by using small circular paths inside of this domain, see Figure 3.

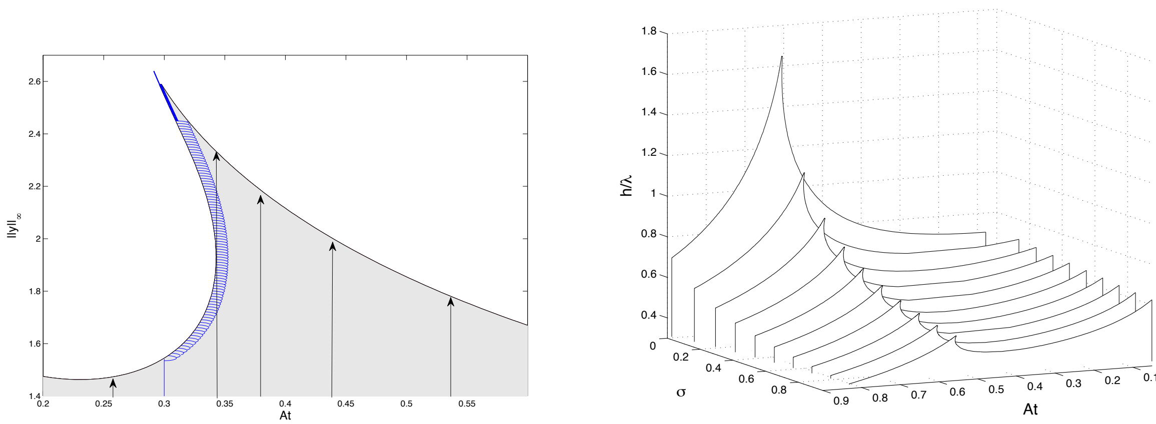

Figure 3: **Left:** The trajectories of the two continuation methods used to determine where traveling waves exist are depicted. The vertical arrows denote continuation paths used with the MAQS algorithm of Section 4.1. The increasingly small circles near the boundary denote a continuation path taken by BCM. **Right:** The location of the largest traveling wave is traced using the BCM, in displacement and Atwood number, for a variety of Bond numbers. The origin is in the back right corner of this figure, for display purposes. These boundaries are observed to generically resemble breaking waves (in that they overturn).

4.1 Sampling Methodology

In this section we describe a sampling method used to adaptively select points (values of Atwood ratio, Bond number and mean shear) for which branches of traveling waves of varying amplitude are computed. This method is used to efficiently probe the full four-dimensional parameter space of traveling waves. This is in contrast to the method presented in section 4.2, which is designed to compute only boundaries of this space.

The sampling methodology is based on a multidimensional adaptive quadrature routine over simplices (MAQS) [39, 40]. The method is designed for high dimensional quadrature; we apply it here to two-dimensional domains. For example, the results of one application of this procedure are in Figure 3, where in we fix Bond number, and adaptively sample values of mean shear and Atwood ratio. The function we sample is the displacement of the largest wave on a branch of traveling waves with fixed values of At, σ, and γ_0; for each parameter choice we continue in displacement to the largest wave and report its value of h. This adaptive routine uses linear function approximations over triangular elements in an adaptively refined mesh. The adaptive refinement is based on an estimate of the error in the sample over the given triangle. In this case, the error is estimated as the absolute value of the difference between a linear and quadratic approximation of the function over a given triangle, or simplex. The algorithm creates a priority queue of the simplices, based on the size and estimated error associated with each simplex. The algorithm then proceeds to process (subdivide) the simplex associated with the highest priority. This process is repeated until the required error tolerance or other stopping criteria (e.g. maximum number of function evaluations) is met.

The function estimate is based on multivariate Lagrange interpolation in the spirit of [41]. This

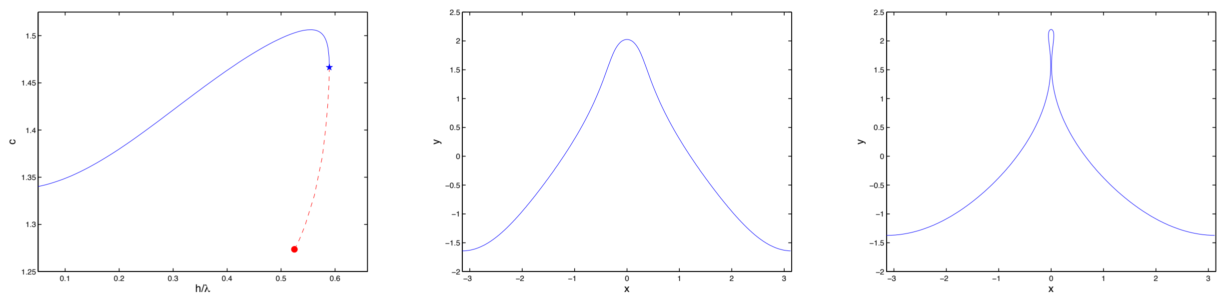

Figure 4: The wave speed of a branch of traveling waves is depicted as a function of the scaled total displacement. The speed has a turning point, so computing this branch requires two continuation parameters. The wave with the largest displacement is marked with a star; its profile is in the center panel. The branch terminates in a self intersecting profile, with smaller total displacement, whose speed is marked with a circle on the left, and is depicted in the rightmost panel. These waves all have At$= 0.565$, $\gamma_0 = 0.5$, and $\sigma = 0.5$.

allows function evaluations to be used and reused until the algorithm has terminated. Additionally, each simplex can be processed independently, which allows for the parallel processing of multiple high error simplices at once. More information on the sampling method, as well as its error estimations and convergence properties are in [39], other competitive sampling algorithms are discussed in [42].

4.2 Boundary Continuation Method (BCM)

In addition to the adaptive sampling algorithm described in the previous section, we also implemented a continuation method specifically to compute the boundaries of the space where traveling waves exist. The sampling method in the previous section computes trajectories in parameter space where h varies and $(\sigma, \mathrm{At}, \gamma_0)$ are fixed. This method does not require that the maximal displacement be continuous, but does require that the boundary is a function of $(\sigma, \mathrm{At}, \gamma_0)$. We observe the opposite to be the case. The boundaries are continuous, but are not single-valued functions of $(\sigma, \mathrm{At}, \gamma_0)$, see Figure 3. Based on this observation we also compute these boundaries by a continuation method (BCM) described below.

BCM begins by computing one trajectory to the boundary from $h = 0$. After one point on the boundary has been approximated, traveling waves are computed on an arc of a circle in parameter space, within the domain of existence of traveling waves. The computed boundary point is used as the center of the arc, the radius is fixed. The angle on the arc is used as the continuation parameter. When a new boundary point is computed along the arc, this point is used as the center of the next circle and the procedure is repeated. This procedure computes points on the boundary until either a maximum number of points are reached, the entire boundary is computed, or the boundary has a cusp. The third criteria is tested by checking the change in the tangent vector of the the computed boundary: if the change in tangent angle is larger than $\pi/3$, the radius of the circles is decreased, and the procedure continues with smaller arcs.

The boundary continuation method involves additional assumptions over the sampling method of the previous section. Both methods assume that the traveling waves are jointly continuous in all

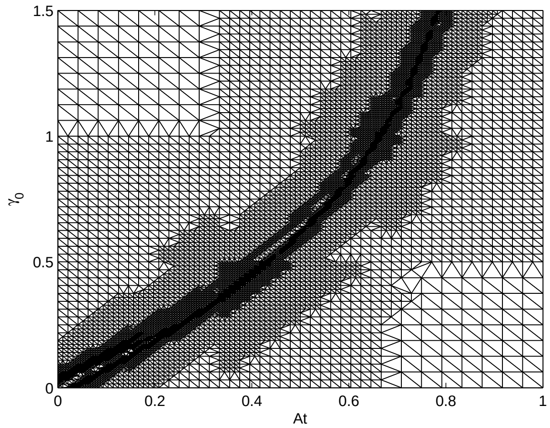

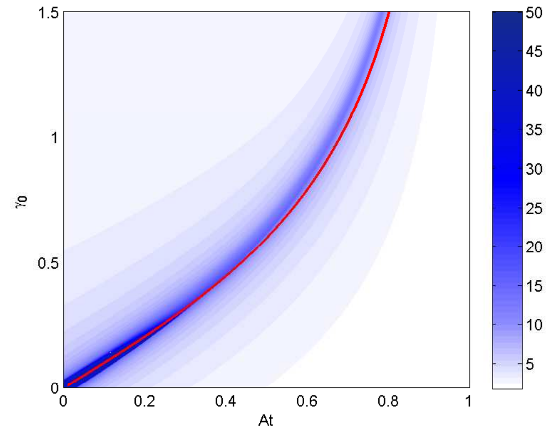

Figure 5: **Left:** The adaptive grid generated using the MAQS algorithm with $\sigma = 0$. **Right:** The largest wave amplitude computed using continuation paths along which only h varies, and γ_0 and At are sampled using the MAQS algorithm. The curve where $d_1 = 0$ is marked with a solid line. Darker shading corresponds to larger total displacement, h.

four parameters. The boundary continuation method also assumes that the region, in parameter space, in which these traveling waves exist, is simply connected (so that it has a single continuous boundary). The previous sampling method does not make such an assumption, in fact should the boundary not be continuous, or not a single valued function of amplitude, it computes the lowest points on the boundary as a discontinuous function of the other parameters (Atwood number, Bond number and mean shear). The trajectories of each method are reported the left panel of Figure 3, where the BCM computes traveling waves on circles near the boundary, and the adaptive sampling method computes traveling waves along adaptively chosen vertical lines. Both methods should be used when exploring parameter space: BCM for the computation of the boundary (since it is both less expensive, scaling in cost like the length of the boundary, and can compute overturning boundaries), and the adaptive sampling method (to verify the the region below the boundary is simply connected and to provide information on the location and the number of cusps).

5 Numerical Results

In this section we discuss the subsets of our four dimensional parameter space, At, σ, h, and γ_0, for which we have computed traveling waves. We focus on computing the extremal values of displacement h for which solutions exist, for each value of Atwood ratio At, mean shear γ_0 and Bond number σ. We consider both pure-capillary ($\sigma = 0$) and capillary-gravity ($\sigma \neq 0$) internal waves ($0 \leq \mathrm{At} < 1$). We consider $\sigma < 1$, so as to stay away from the Wilton ripple resonance, beginning at $\sigma = \frac{1}{\mathrm{At}}(1 + \gamma_0^2)$, see equation (9). All of the computed waves are of the Stokes' type. At each value of $(\sigma, \mathrm{At}, \gamma_0)$, we compute largest wave profiles and the simply-connected regions of parameter space in which traveling waves exist. We compute the boundaries of these regions using BCM. We verify that these regions are simply connected using the adaptive sampling algorithm (MAQS).

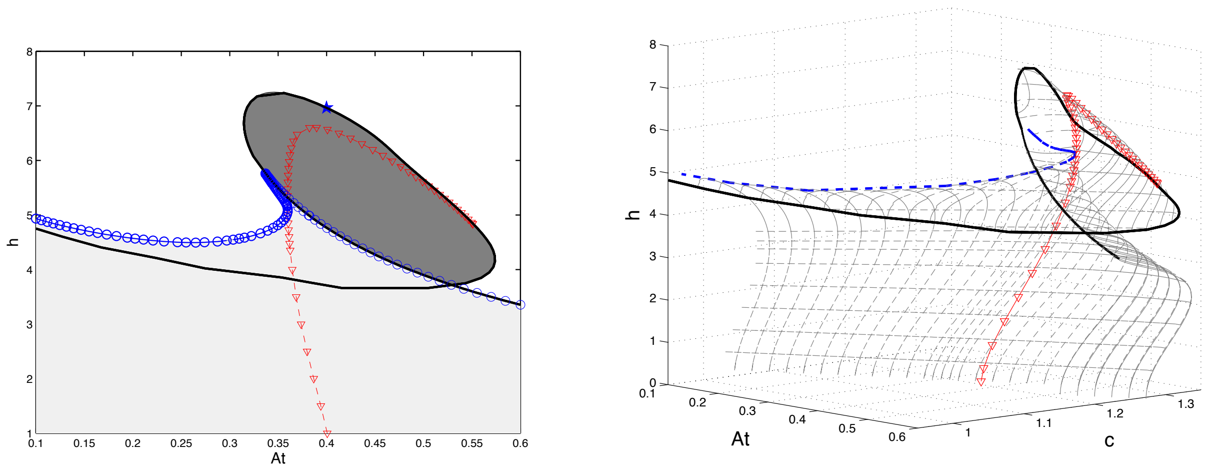

Figure 6: **Left:** The region where traveling waves exist in Atwood number and displacement. The lighter gray region corresponds to that which is reported in Figure 3, its boundary (marked with circles) is the wave of maximal displacement on a branch. The thick black curve (in both panels) is the location of self-intersecting waves as computed using the BCM. The dark gray region is that which cannot be computed with continuation only in amplitude, but does correspond to regular wave profiles. The doubly self-intersecting profile in Figure 7 is marked with a star. **Right:** The surface where traveling waves solutions exist is visualized in Atwood number (At), speed (c), and total displacement (h). The surface is folded along the dashed (blue) curve, which in the left panel is marked by the circles which lie to the left of the cusp. The amplitude of self intersection is marked with the solid thick black curve. Waves whose second harmonic vanishes are marked red triangles. Both panels compute waves with mean shear $\gamma_0 = 0.5$ and Bond number $\sigma = 0.5$.

We observe that there are two boundaries of interest in this problem. First, we compute the amplitude for which traveling waves self intersect, which is necessarily at the end of a branch of traveling waves. Second, we compute the extremal amplitude of a branch of traveling waves (fixing At,σ, and γ_0), which we observe to occur sometimes at self-intersecting waves, and sometimes at turning points, see Figure 4.

When tracing the largest displacement, we observe that this boundary has a cusp somewhere between At $= 0$ and At $= 1$. To compute this cusp, we use two runs of BCM (once increasing At from zero, once decreasing At from 1). Both applications detect the presence of the cusp, and adaptively decrease the radius of the BCM circles until a prescribed tolerance is reached. In this way the procedure computes boundaries which are C^0 (but need not be C^1). The adaptive circle radius was designed specifically for this case, where the boundary has a single cusp; however, it would be simple to extend the algorithm to compute boundaries with more cusps.

The largest displacement h along a branch, as a function of mean shear and Atwood number, is reported for $\sigma = 0$ in the right panel of Figure 5. In this panel, the parameter values where the coefficient d_1 (the coefficient the second harmonic tangent angle in a Stokes expansion) changes sign are marked with a solid curve. For $\sigma = 0$, the region within which traveling waves exist has a boundary which is a function of both At and γ_0. This boundary is observed to have a cusp, near the zero of d_1, which marks the location where the self intersecting wave transitions from entraining bubbles in the upper fluid to the lower fluid. The agreement of the cusp with the root of d_1 is not exact, but considering that d_1 is a small amplitude property it is quite remarkable that it is able to make any prediction about bubble entrainment at all (this being a large amplitude property). Figure 5 was generated using the adaptive sampling algorithm, continuing only in displacement.

For non-zero Bond numbers, the wave of largest displacement for fixed physical parameter values $(\mathrm{At}, \gamma_0, \sigma)$ often occurs at a turning point. In this setting, the displacement h of the largest traveling wave on a branch is not a single valued function of the At, σ or γ_0. If we continue only in the physical parameters and displacement, applying the boundary continuation algorithm computes a single wave at each set of parameter values, resulting in Figure 3. The boundaries of the computed regions themselves resemble overturned waves - as is also depicted in 3. The extent to which these boundaries overturn increases with Bond number (the boundary does not overturn for $\sigma = 0$). Figure 3 takes mean shear $\gamma_0 = 0.5$, other values of mean shear have similar boundaries. We observe that the computed boundaries depend continuously on mean shear and Atwood ratio, and Bond numbers, but overturn for all non-zero Bond numbers. Many of the computed waves with maximal displacements are regular. These waves cannot correspond to the end of the branch of traveling waves (see the global bifurcation theorem of [1]); they are at turning points. An example branch of traveling waves where the wave of maximal displacement is neither self-intersecting nor the end of the branch is depicted in Figure 4.

When the wave of maximal displacement on a branch is regular, the branch terminates with a self-intersecting profile, after a turning point. We have applied the boundary continuation algorithm to trace the location of self-intersecting waves (regardless of whether they are the wave of maximal displacement). We observe that the location of these self-intersecting waves (in parameter space) is itself self-intersecting, at least when projected into the Atwood number/displacement plane, see the left panel of the Figure 6. For $\sigma = 0.5$ and $\gamma_0 = 0.5$, we have computed the entire surface on which traveling waves exist by continuation inward from the two "boundaries" (of maximal displacement and of self-intersection) computed with the BCM. This surface is visualized in the three-dimensional space of Atwood number, speed, and total displacement in the right panel of Figure 6.

Of particular interest in Figure 6 is the dark grey region in the left panel. For the Atwood numbers below this region, approximately $\mathrm{At} \in (0.35, 0.55)$, branches of traveling waves parameterized by displacement do not have turning points, and terminate in self-intersecting waves whose displacements are marked by circles. Using BCM to follow the location of self intersecting waves we see that for these Atwood ratios, there are two values of h at which there is a self intersecting profile. The larger profile is on the same surface as the smaller one, but is not on the same branch of traveling waves for *fixed* Atwood ratio. This upper branch of traveling waves is near to having two-self intersections, at both the crests and troughs. We believe that only one wave has self-intersection at both places; an approximation of this wave is in Figure 7.

In section 3, we presented the small amplitude asymptotics of Stokes' waves. From these asymptotics, we observe that the sign of d_1 predicts whether small amplitude waves have steeper troughs or crests. This small amplitude property is often preserved along a branch: when small amplitude waves have steeper troughs, they culminate in a bubble at the crest (and vice versa when the small amplitude wave has steeper trough). This heuristic does not actually predict the location where the self-intersecting wave switches from entraining a bubble in the upper to lower fluid. This can be seen in the right panel of Figure (5), where the location of the largest waves is slightly offset

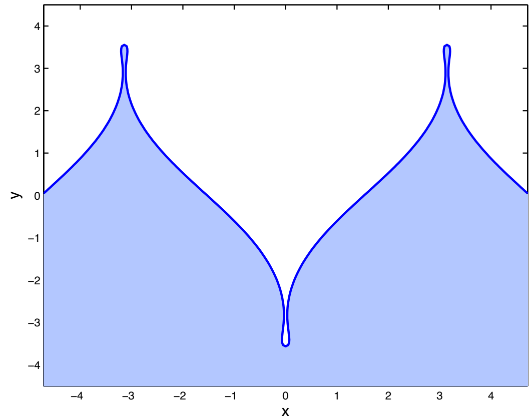

Figure 7: At the transition, in parameter space, between waves which entrain a bubble into the lower fluid and the upper fluid is a wave which entrains bubbles into both fluids. Above is a regular wave in the neighborhood of such a doubly self-intersecting configuration. This configuration is marked with a star in Figure 6

from the curve where $d_1 = 0$.

In addition, in Figure 6 we plot the parameter values where the second harmonic of the finite amplitude waves vanish, $\hat{y}(k = 2) = 0$, marked with triangles. This curve connects to the point at zero amplitude where $d_1 = 0$, and traces the trajectory in parameter space where the finite amplitude traveling waves have zero second harmonic. We observe that self-intersecting profiles with bubbles on both the troughs and crests exist at parameter values on both sides of this curve, just as they live on both sides of the parameter values where $d_1 = 0$. Thus this extension of the previous heuristic based on d_1 is also not predictive regarding the character of self-intersection.

For a general cross section of parameters, the large amplitude waves with zero second harmonic are not the globally largest waves. In Figure 6 one can observe that the globally largest wave does not lie on the curve with zero second harmonic (marked with triangles). The globally largest wave also does not entrain bubbles/drops into both fluids (as was the case in [5]). The wave which entrains bubbles into both fluids is marked with a star in Figure 6 and is depicted in Figure 7.

6 Conclusion

In this work we compute overturning traveling capillary-gravity waves on the interface between two constant-density fluids. We compute branches which can be parameterized by displacement, as well as those with turning points. Global branches of traveling waves are computed, including those which connect flat state configurations at two different speeds, illustrating the theorem of [1]. We trace the location of traveling waves of extremal displacement and as well as the locations of self-intersecting waves, in parameter space, in both cases using numerical continuation methods. These two curves are themselves overturning and self-intersecting respectively. We also evaluate the heuristic that branches of waves which have steeper troughs at small amplitudes might terminate with a bubble at their trough, while branches of waves that have steeper crests are small amplitude might terminate at a wave with a bubble on its crest. We observe that although this heuristic performs admirably, it is not the truth.

Our methods require regular profiles, and can compute profiles only in the limit approaching self-intersection. Amending our method to compute waves which self intersect (coupled to a specification of the pressure within any bubbles) would allow us to compute larger waves. A second future research area is the overturning structure of Wilton ripples, and their internal wave counterparts (both surface tension and shear based). We are also currently pursuing extension of this method to three-dimensions as well as computing the spectral stability of overturned traveling waves for both two and three-dimensional fluids.

Acknowledgements: This work was partially supported by a grant from the Simons Foundation (#313852 to Benjamin Akers). DMA gratefully acknowledges support from the National Science Foundation through grant DMS-1016267. JDW gratefully acknowledges support from the National Science Foundation through grants DMS-0908299 and DMS-1105635.

References

[1] D.M. Ambrose, W.A. Strauss, and J.D. Wright. Global bifurcation theory for periodic traveling interfacial gravity-capillary waves. *Ann. Inst. H. Poincare Anal. Nonlineaire*, 2015. Accepted.

[2] P.G. Saffman. *Vortex dynamics*. Cambridge Monographs on Mechanics and Applied Mathematics. Cambridge University Press, New York, 1992.

[3] B. Akers, D.M. Ambrose, and J.D. Wright. Traveling waves from the arclength parameterization: Vortex sheets with surface tension. *Interfaces and Free Boundaries*, 15:359–380, 2013.

[4] B. Akers and P.A. Milewski. A model equation for wavepacket solitary waves arising from capillary-gravity flows. *Studies in Applied Mathematics*, 122(3):249–274, 2009.

[5] B.F. Akers, D.M. Ambrose, and J.D. Wright. Gravity perturbed crapper waves. *Proceedings of the Royal Society of London, Series A*, 470(2161), 2014.

[6] G.D. Crapper. An exact solution for progressive capillary waves of arbitrary amplitude. *J. Fluid Mech.*, 2:532–540, 1957.

[7] P. de Boeck. Existence of capillary-gravity waves that are perturbations of Crapper's waves. 2014. Preprint. arXiv:1404.6189.

[8] D. Cordoba, A. Enciso, and N. Grubic. Splash and almost-splash stationary solutions to the Euler equations. 2014. Preprint. arXiv:1412.7382.

[9] A. Constantin and W. Strauss. Exact steady periodic water waves with vorticity. *Comm. Pure Appl. Math.*, 57(4):481–527, 2004.

[10] R.E.L. Turner and J.-M. Vanden-Broeck. The limiting configuration of interfacial gravity waves. *Phys. Fluids*, 29:372–375, 1986.

[11] R.E.L. Turner and J.-M. Vanden-Broeck. Broadening of interfacial solitary waves. *Physics of Fluids (1958-1988)*, 31(9):2486–2490, 1988.

[12] M. Debiane and C. Kharif. A new limiting form for steady periodic gravity waves with surface tension on deep water. *Physics of Fluids*, 8:2780, 1996.

[13] M. Debiane, C. Kharif, and M. Amaouche. A new method for the calculation of steady periodic capillary-gravity waves on water of arbitrary uniform depth. *European Journal of Mechanics-B/Fluids*, 19(6):855–870, 2000.

[14] H. Okamoto and M. Shōji. *The mathematical theory of permanent progressive water-waves*, volume 20 of *Advanced Series in Nonlinear Dynamics*. World Scientific Publishing Co. Inc., River Edge, NJ, 2001.

[15] J.-M. Vanden-Broeck and J.B. Keller. A new family of capillary waves. *Journal of Fluid Mechanics*, 98:161–169, 5 1980.

[16] E. Parau and F. Dias. Interfacial periodic waves of permanent form with free-surface boundary conditions. *Journal of Fluid Mechanics*, 437:325–336, 2001.

[17] G. Iooss. Gravity and capillary-gravity periodic travelling waves for two superposed fluid layers, one being of infinite depth. *J. Math. Fluid Mech.*, 1(1):24–61, 1999.

[18] C.G. Koop and G. Butler. An investigation of internal solitary waves in a two-fluid system. *Journal of Fluid Mechanics*, 112:225–251, 1981.

[19] H. Michallet and E. Barthelemy. Experimental study of interfacial solitary waves. *Journal of Fluid Mechanics*, 366:159–177, 1998.

[20] J. Grue, A. Jensen, P.-O. Rusås, and J.K. Sveen. Properties of large-amplitude internal waves. *Journal of Fluid Mechanics*, 380:257–278, 1999.

[21] H. Segur and J.L. Hammack. Soliton models of long internal waves. *Journal of Fluid Mechanics*, 118:285–304, 1982.

[22] O. Laget and F. Dias. Numerical computation of capillary–gravity interfacial solitary waves. *Journal of Fluid Mechanics*, 349:221–251, 1997.

[23] J.W. Choi, S.M. Sun, and M.C. Shen. Internal capillary-gravity waves of a two-layer fluid with free surface over an obstruction?forced extended kdv equation. *Physics of Fluids (1994-present)*, 8(2):397–404, 1996.

[24] R.H.J. Grimshaw and D.I. Pullin. Extreme interfacial waves. *Physics of Fluids (1958-1988)*, 29(9):2802–2807, 1986.

[25] D.I. Pullin and R. Grimshaw. Interfacial progressive gravity waves in a two-layer shear flow. *Physics of Fluids (1958-1988)*, 26(7):1731–1739, 1983.

[26] Y. Mark and T. Miloh. On periodic solutions of interfacial waves of finite amplitude. *European Journal of Mechanics-B/Fluids*, 49:58–64, 2015.

[27] S.A. Thorpe. On the shape of progressive internal waves. *Philosophical Transactions for the Royal Society of London. Series A, Mathematical and Physical Sciences*, pages 563–614, 1968.

[28] Y. Tsuji and Y. Nagata. Stokes' expansion of internal deep water waves to the fifth order. *Journal of the Oceanographical Society of Japan*, 29(2):61–69, 1973.

[29] W.J. Harrison. The influence of viscosity and capillarity on waves of finite amplitude. *Proceedings of the London Mathematical Society*, 2(1):107–121, 1909.

[30] V.D. Djordjevic and L.G. Redekopp. On two-dimensional packets of capillary-gravity waves. *Journal of Fluid Mechanics*, 79(04):703–714, 1977.

[31] D.M. Ambrose. Well-posedness of vortex sheets with surface tension. *SIAM J. Math. Anal.*, 35(1):211–244 (electronic), 2003.

[32] J.-M. Vanden-Broeck. *Gravity-capillary free-surface flows*. Cambridge University Press, 2010.

[33] G.B. Whitham. *Linear and nonlinear waves*, volume 42. John Wiley & Sons, 2011.

[34] B.F. Akers and W. Gao. Wilton ripples in weakly nonlinear model equations. *Commun. Math. Sci*, 10(3):1015–1024, 2012.

[35] W.J. Pierson and P. Fife. Some nonlinear properties of long-crested periodic waves with lengths near 2.44 centimeters. *Journal of Geophysical Research*, 66(1):163–179, 1961.

[36] C.G. Broyden. A class of methods for solving nonlinear simultaneous equations. *Math. Comp.*, 19:577–593, 1965.

[37] B. Akers and P.A. Milewski. Dynamics of three-dimensional gravity-capillary solitary waves in deep water. *SIAM Journal on Applied Mathematics*, 70(7):2390–2408, 2010.

[38] J.-M. Vanden-Broeck and F. Dias. Gravity-capillary solitary waves in water of infinite depth and related free surface flows. *J. Fluid Mech*, 240:549–557, 1992.

[39] K.R. Pond. *Multidimensional Adaptive Quadrature Over Simplices*. PhD thesis, Virginia Polytechnic Institute and State University, 2010.

[40] Jeff Borggaard, Kevin R Pond, and Lizette Zietsman. Parametric reduced order models using adaptive sampling and interpolation? In *World Congress*, volume 19, pages 7773–7778, 2014.

[41] T. Sauer and Y. Xu. On multivariate Lagrange interpolation. *Mathematics of Computation*, 64(211):1147–1170, 1995.

[42] J.N. Lyness and J.J. Kaganove. Comments on the nature of automatic quadrature routines. *ACM Transactions on Mathematical Software (TOMS)*, 2(1):65–81, 1976.